# The retinotopic organization of striate cortex is well predicted by surface topology

Supplemental Information

Noah C. Benson[1,2], Omar H. Butt[1], Ritobrato Datta[1], Petya D. Radoeva[1], David H. Brainard[2], and Geoffrey Karl Aguirre[1]*
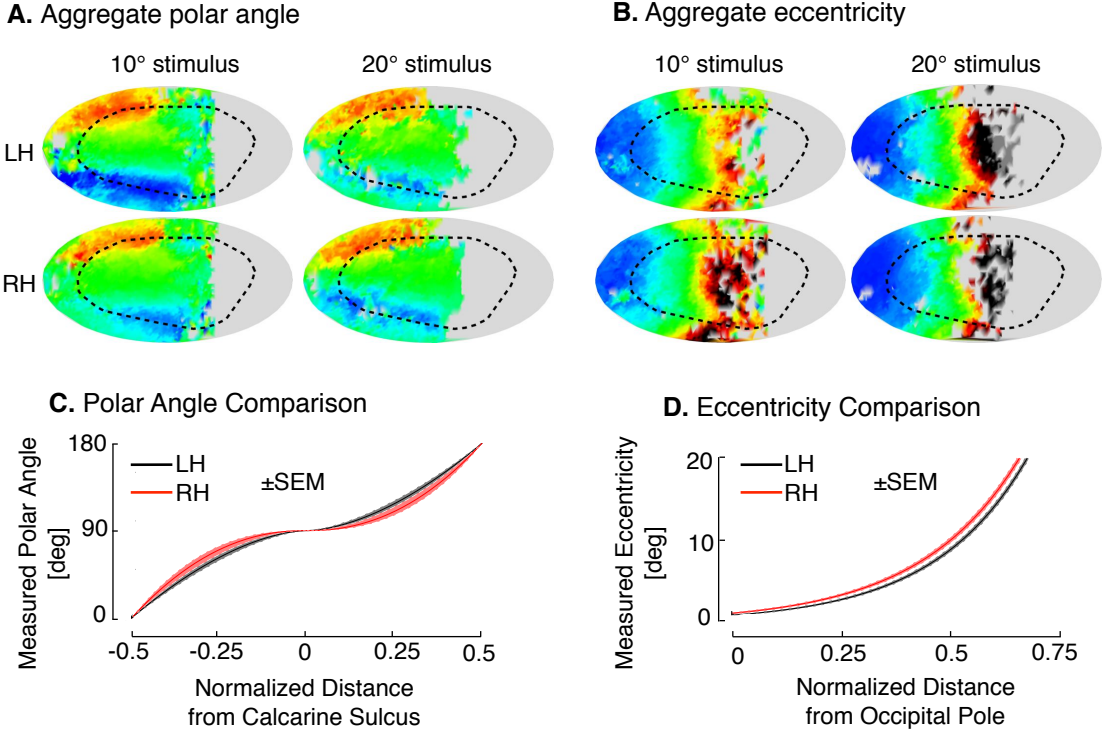
Depts. of [1]Neurology and [2]Psychology, University of Pennsylvania, Philadelphia, 19104

Figure S1. Projection of a visual grid onto the cortical surface, related to Figure 1
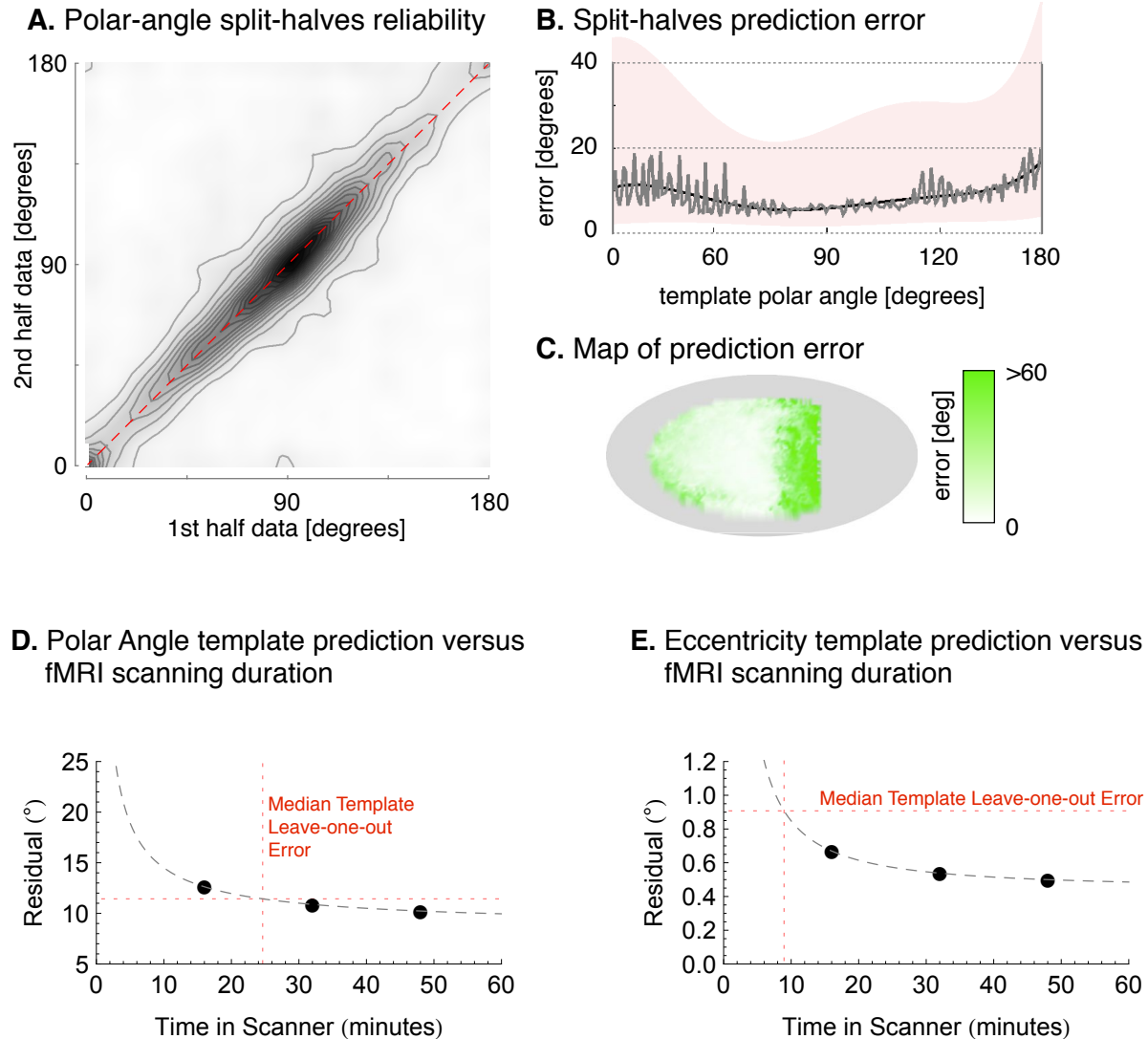

A. Visual grid

B. Projected grid
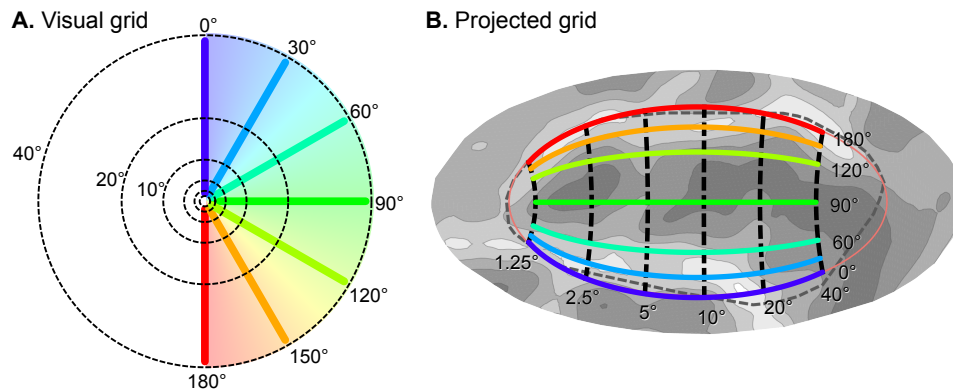
Figure S1. Figure 1 presents the projection of retinotopic mapping data onto a patch of cortical surface containing striate cortex. Shown here is a projection of the visual field (A) onto the cortical surface (B). The parameters of the projection are derived from the measurements given in Table S1, for the combined left-right hemisphere. Note that some of the apparent magnification about the horizontal meridian is a consequence of expansion of the cortical surface along the depths of the calcarine sulcus during cortical inflation and projection to a two-dimensional surface.

Figure S2. Hemispheric comparison, related to Figures 2 and 3.

A. Aggregate polar angle

B. Aggregate eccentricity

C. Polar Angle Comparison

D. Eccentricity Comparison

Figure S2. (**A**) Polar angle and (**B**) eccentricity aggregate data for the left and right hemispheres of all subjects shown stimuli out to 10° and 20° of eccentricity. (**C**) The average across subject polar angle and (**D**) eccentricity template fits, plotted as a prediction of polar angle or eccentricity against a normalized iso-eccentric or iso-angular axis. Data is plotted in black/gray for the left hemisphere, and red/pink for the right hemisphere.The thick lines indicate the template predictions in terms of normalized distance from the calcarine sulcus (polar angle) and the occipital pole (eccentricity) while the shaded regions indicate standard errors across the population of 25 subjects.

Figure S3. Split-halves reliability of polar angle and template versus scan prediction, related to Figure 4.

A. Polar-angle split-halves reliability

B. Split-halves prediction error

C. Map of prediction error

D. Polar Angle template prediction versus fMRI scanning duration

E. Eccentricity template prediction versus fMRI scanning duration

Figure S3. (A) Contour histogram of all vertices for the 10° dataset determined by calculation of polar angle separately for each half of the fMRI scan. Each contour line corresponds to ~4,100 vertices **(B)** Median absolute split-halves error across vertices and subjects by template eccentricity. The median error (grey), is fit by a fifth-order polynomial (black) with the similarly fit upper and lower quartiles defining the border of the pink region. **(C)** Test-retest absolute residuals between first- and second-half measurements for each vertex shown on the cortical surface.

The lower two panels present the median absolute error (*y*-axis) in measurement of **(D)** polar angle and **(E)** eccentricity derived from an fMRI, retinotopic mapping session of a given duration

(*x*-axis) as determined by comparison to a separate, 48 minute scan from the same individual. A decaying polynomial of the form $c_1 + c_2\,x^{-k}$ was fit to the data and is plotted with a dashed black line. The performance of our template across the population of 19 other subjects shown stimulus out to 10° of eccentricity is indicated by a dotted red cross-hairs, the *y*-value of which indicates the median absolute leave-one-out error from the template (made with all but one subject) to the left-out subject. The corresponding *x*-value indicates the amount of scanner time required in the example subject to obtain a precision of retinotopic mapping equivalent to the anatomical, template approach.

Table S1. Exact template formulae and leave-one out prediction errors for left, right, and combined hemispheres, related to Figures 2 and 3.

Polar Angle	Left Hemisphere	Right Hemisphere	Both Hemispheres
Formula	$90° + 90° \, \mathrm{sgn}(x) \, |x|^{1.44}$	$90° + 90° \, \mathrm{sgn}(x) \, |x|^{1.96}$	$90° + 90° \, \mathrm{sgn}(x) \, |x|^{1.71}$
Median Error	12.29°	10.65°	11.43°
Error Range [a]	5.49° - 23.34°	4.78° - 33.83°	4.78° - 33.83°
Eccentricity	Left Hemisphere	Right Hemisphere	Both Hemispheres
Formula	$90° \exp(4.70(x - 1))$	$90° \exp(4.39(x - 1))$	$90° \exp(4.57(x - 1))$
Median Error	0.93°	0.88°	0.91°
Error Range [a]	0.60° - 1.56°	0.46° - 2.68°	0.46° - 2.68°
Posterior Intercept [b]	0.98°	1.01°	0.99°

[a] The Error Range reports the minimum and maximum median absolute error of all subjects; note that this is not the same as the Median Error, which reports the median absolute error of all vertices.

[b] The posterior intercept is the template's predicted eccentricity value at the posterior end of V1 near the foveal confluence.

Supplemental Experimental Procedures

Subjects

 A total of 25 people participated in retinotopic mapping experiments (15 females, ages 20 to 42; mean 24). Participants had normal or corrected-to-normal visual acuity and were screened to exclude those who had recently taken COX-1 inhibitors. The study was approved by the University of Pennsylvania Institutional Review Board, and all subjects provided written informed consent. The retinotopic mapping data from each subject may be downloaded (http://cfn.upenn.edu/aguirreg/public/V1/BensonNC_2012_CurrBiol.tar.gz), and all code used in this paper for the analysis and plotting of these data are included in the supplemental Mathematica notebook, which has been written to dynamically download and analyze our data via this website by default.

Stimuli

 Stimuli were generated on an Apple MacBook (OSX 10.5.8) using in-house custom-made Matlab™ (Mathworks, Inc.) codes augmented by the mgl (http://justingardner.net/doku.php/mgl/overview) and Psychtoolbox (http://psychtoolbox.org) display routines, and were presented onto a rear-projection Mylar screen from a projector with Buhl long-throw lenses. Subjects viewed the screen through a head-coil mounted mirror (124.25 cm distant from the screen) mounted over the right eye. Separate subjects were studied using two different retinotopic mapping protocols.

 A first, 10° dataset was collected using a single sweeping bar of 2.5º thickness which flickered at 5 Hz, based on the stimuli of Dumoulin and Wandell [1]. The bar traveled within a central 20° aperture in 4 orientations: horizontal, vertical, angled +45º and angled -45º. For three subjects, the bar remained in a given position for a period of 6 s before shifting in 2.5º steps. For these subjects, stimulation occurred for a given orientation in 8 discrete steps. For the remainder of the subjects, the bar shifted by 1.25º every 3s. For these subjects, there were 17 steps per orientation. For both stimulation protocols, individual scans consisted of 2 orientations (0°/90° and 45°/-45°) with 4 spatial sweeps for each plus periods of mean background luminance. There were no reversals, and individual sweeps always proceeded in the same spatial direction (top to bottom, right to left, etc.). For all subjects, total bar mapping stimuli consisted of ~27 minutes divided into 4 individual scans of two cardinal bars and two angled bars. Finally, a single subject was scanned using a 1.25º shifting bar stimuli with reversals for 96 minutes. Subjects were instructed to fixate the center of the screen, which was indicated by four small radially oriented red arrows placed at ~2º of eccentricity and at 45º, 135º, -45º, and -135º of polar angle. To help maintain fixation, all subjects completed a stimulus-unrelated attention task consisting of a bilateral button-press in response a random flicker of the fixation stimulus.

 A separate group of 6 subjects were studied for the 20° dataset using standard "ring and wedge" stimuli [2]. Unlike in the bar-stimulus studies, subjects directed their gaze to an eccentric fixation point, resulting in visual stimulation of one hemifield with a greater range of eccentricity. An expanding ring (2 Hz flickering, black-and white checkerboard on a gray background) was used to map the eccentricity representation. The subjects

fixated on a red dot, presented 0.04° from the left edge of the screen, while the ring expanded into the periphery of the right hemifield, in 16 eccentricity steps, each lasting 3 s. Subjects monitored for an occasional flicker of the fixation stimulus and were instructed to make a bilateral button-press in response. The ring width varied exponentially with eccentricity and ranged from 0.6º to 6.7° of visual angle. The annulus completed 10 cycles of expansion during each scan (scan time = 10 × 48 s = 8 min.). A rotating 22.5° wedge (also 2 Hz flickering checkerboard) was used to map polar angle. The wedge rotated clockwise and traversed one hemifield in 48 s (16 steps of 3 s/TR). To minimize light-scatter during collection of the 20° dataset, the bore of the scanner was covered in black matte fabric, as was the head-coil. Sixty-four minutes of RM data was collected each with right and left visual field stimulation for each subject.

Magnetic Resonance Imaging

Scans were acquired using a 3-Tesla Siemens Trio with a standard 8-channel Siemens head coil. Echoplanar BOLD fMRI data was collected with a TR of 3 s, with 3 × 3 × 3 mm isotropic voxels with 42 axial slices, in an interleaved fashion with 64 × 64 voxel in-plane resolution, and with whole brain coverage. Head motion was minimized with foam padding. Continuous pulse-oximetry was recorded for most scanning sessions. A standard T1-weighted, high-resolution anatomical scan of Magnetization Prepared Rapid Gradient Echo (3D MPRAGE) (160 slices, 1 × 1 × 1 mm, TR = 1.62 s, TE = 3.09 ms, TI = 950 ms, FOV= 250 mm, FA = 15°) was acquired for each subject. For those subjects whose data was acquired over multiple scanning sessions, the individual MPRAGE images from each session were aligned and averaged prior to tissue segmentation and analysis in FreeSurfer.

Image pre-processing

Data were sinc interpolated in time to correct for the slice acquisition sequence and motion corrected with a six-parameter, least squares rigid body realignment routine using the first functional image as a reference.

Initial statistical analysis used a finite-impulse-response basis of shifted delta functions to model neural response to the stimulus positions. The BOLD signal was modeled with a population average hemodynamic response function (HRF) [3] (for the 10° dataset) or with a subject-specific HRF derived from a separate, blocked visual stimulation scan (for the 20° dataset). Nuisance covariates included effects of scan, global signals, spikes (periods of raw signal deviation greater than two standard deviations from the mean), and cardiac and respiratory fluctuations (when available). The latter were derived from raw, 50 Hz pulse-oximetry measurements taken during BOLD scanning. After aligning raw pulse data with DICOM image timestamps, raw pulse arrays were split into high (cardiac) and low (respiratory) frequency covariates using software (https://cfn.upenn.edu/aguirre/wiki/public:pulse-oximetry_during_fmri_scanning) derived from the PhLEM toolbox (http://sites.google.com/site/phlemtoolbox/) [4].

Anatomical data were processed using the FMRIB Software Library (FSL) toolkit (http://www.fmrib.ox.ac.uk/fsl/) to correct for spatial inhomogeneity and to perform non-linear noise-reduction. Brain surfaces were reconstructed and inflated from the MPRAGE images using the FreeSurfer toolkit (http://surfer.nmr.mgh.harvard.edu/) [5-7].

Individual whole brain (right & left hemisphere) surface maps were then registered to a common FreeSurfer template surface, pseudo-hemisphere (fsaverage_sym) using the FreeSurfer spherical registration system [8,9]. With minimal metric distortion, this approach matches morphologically homologous cortical areas based on the cortical folding patterns, then resamples individual results to a standard (fsaverage_sym) surface. The resulting pseudo-hemisphere surface representation is composed of a network of vertices that align at a sub-voxel resolution to the volumetric anatomy both between subjects, and between hemispheres.

Probabilistic boundaries of V1 was defined using an average atlas definition for V1 [10] in the reconstructed brain surface of 42 subjects (who contributed only anatomical images) with demographics comparable to that of our retinotopic mapping subject population. Individual right and left V1 surface boundaries were resampled to the standard (fsaverage_sym) surface, then averaged. The standard surface's V1 boundary was set at the 50% threshold of the resulting 84 (42 left and 42 right hemisphere) V1 boundaries. The echoplanar data in subject space were co-registered to the subject specific anatomy in FreeSurfer using FSL-FLIRT with 6 degrees of freedom under a FreeSurfer wrapper (bbregister).

Calculation of retinotopic mapping values

For the 10° dataset—which made use of sweeping bar stimuli—polar angle and eccentricity values for each voxel were defined using the population receptive field (pRF) approach [1]. In order to fit a pRF model to each voxel we searched the central $26° \times 26°$ square centered at the point of fixation, using 0.25° intervals and receptive field sizes ranging from 0.2 - 3°. In all, 165,327 pRF models, which also included the predictor matrix containing all nuisance covariates, were tested on a voxel-by-voxel basis against the raw signal, which was filtered to remove frequencies below the stimulus frequencies. An F-test of the best fit model (compared to a mean model) was also recorded for significance weighting.

Misspecification of the phase of the HRF causes bias in the assigned retinotopic values for individual subjects (although this would not systematically bias aggregate template fits if the HRF correctly reflects the central tendency of the population). To minimize this error, the fitting routine also tested phase-shifted (± 2 s) versions of the average HRF in 1 s increments. The use of cardinal and oblique orientations in the bar stimuli enforces a unique HRF phase solution that will best fit both sweep directions. The shift producing the lowest residual sum of squares over all V1 voxels was selected as the HRF delay for each subject.

Resulting polar angle, eccentricity and F-statistic volumes were then registered to the subject-specific anatomical surface, after which the overlay was resampled to the FreeSurfer fsaverage_sym surface.

For the 20°-dataset, which made use of traditional ring and wedge stimuli, polar angle and eccentricity was determined for each voxel by fitting a Gaussian function to the set of 16 β weights. A visual field position x was assigned to each β weight according to the center of the stimulus corresponding to that weight, and the Gaussian function had the form $c_1 \exp(-c_2(x - c_3)^2) + c_4$. The voxel was then assigned the location corresponding to the peak of the Gaussian (c_3). For the eccentricity data, a log transform was applied to x prior to fitting the Gaussian. Ambiguity in the positional assignment of the last stimulus

in each cycle (that arose because of the manner in which the stimuli wrapped at the end of each cycle) was resolved by fitting the data twice, once with this stimulus assigned to each of its possible positions, and retaining the better fit.

Template Fitting

Prior to template fitting, vertices from the dilated V1 region of each subject, as registered to the fsaverage_sym surface, were converted from 3D surface coordinates to a local 2D map (i.e., latitude and longitude). **Figure 1A** shows the fsaverage_sym brain of a single subject after rotation, with V1 outlined. Additionally, a shear transformation was applied to the vertices in the 2D map to reduce the amount of spherical curvature present in the 2D embedding of the data. This overall transformation of a vertex with Cartesian coordinates $(x, y, z)^T$ on the fsaverage_sym brain to $(\varphi, \theta)^T$ in the 2D map is given in the Supplemental *Mathematica* Notebook. The same transformation was applied for each subject, giving identical 2D vertex sets for the probabilistic V1 region in every subject. The resulting V1 projection is shown in **Figure 1B**.

Eccentricity and polar angle organization was defined in a similar fashion to the complex-log transform retinotopy models proposed by Schira *et al.* [11] and Balasubramanian *et al.* [12]. In our model, V1 is an ellipse, and iso-eccentric bands within V1 follow hyperbolas that are orthogonal to the iso-angular bands, which are also ellipses (see **Fig. S1** and the *Mathematica* Notebook for details). Iso-angular bands are upper or lower halves of ellipses with the same center, rotation, and major axis as the V1 ellipse but with a smaller minor axis. Iso-eccentric bands are left or right arms of hyperbolas whose centers are the same as the V1 ellipse's center and whose major axes are parallel to the V1 ellipse's major axis. Each point in V1 was given a coordinate based on the unique iso-angular and iso-eccentric band that passed through it. Eccentricity points were normalized to be 0 at the posterior end of the V1 ellipse and 1 at the anterior end of the V1 ellipse. Polar angle points were normalized to be -1 at the ventral end of the V1 ellipse and 1 at the dorsal end of the V1 ellipse. Although the Schira and Balasubramanian models are excellent descriptions of the organization of V1, we do not use them exactly due to their built-in assumptions about the relationship between V1 shape and organization, their requirement that polar angle and eccentricity be fit simultaneously, and the mathematical intractability of inverting them. Instead, we use their basic organizations as a guide for our template's coordinate system within V1. Full details of the template coordinate system, including algorithms for their calculation, are given in the Supplemental *Mathematica* Notebook.

A distinctive property of the Schira *et al.* [11] model is that it exhibits constant areal magnification along polar angle. Our model implementation is capable of fitting data that has this property, although it does not enforce this constraint. In our data within the template space we used, we did observe a violation of constant areal magnification, which may be appreciated as the "flattening" of the model fit presented in **Fig. 2E**, where measured polar angle changes more slowly per unit change in cortical position close to the horizontal meridian; and in **Fig. S1B** where there is a magnification of representation near the horizontal meridian. At least some of this variation in areal magnification across polar angle is a consequence of the cortical inflation process and projection to a two-dimensional surface, which we confirmed by comparing the surface

areas of equivalent regions of projected visual space in the flattened surface representation and on the folded pial surface. Our templates could be brought into closer agreement with the Schira *et al.* [11] model by enforcing a tighter constraint upon preservation of area in the inflation and flattening process, at the expense of preservation of angular relationships. While it would not improve the anatomically-based predictions of retinotopic mapping values that we pursued here, the resulting template maps would more closely resemble those obtained by, *e.g.*, single unit recording in primates [13].

Measurement bias may arise at the periphery of eccentricity mapping where neurons with large receptive fields are centered beyond the range of the stimulus. For example, a voxel with a receptive field centered at 12±3° could be erroneously assigned an eccentricity of 10°, corresponding to the maximal stimulus eccentricity. More generally, measurement at the border of the mapping stimulus can be biased within the range of receptive field size. Such an effect, appearing as a plateau in the eccentricity function and receptive field sizes at high eccentricities, can be seen in prior RM data sets (*e.g.*, Figure 4 of Press *et al.* [14]; Figure 9 of Dumoulin & Wandell [1]); and has been described as an artifactual "plateau" in eccentricity measurement by Baseler *et al.*, [15]. To avoid this form of bias, we fit our template to the data after excluding those points with a measured eccentricity within 2° of the outer edge of the stimulus. Additionally, voxels in the most-peripheral 25% of V1 were excluded when fitting both eccentricity and polar angle as these voxels were sparse and almost certainly noise; to our knowledge, no model of V1 retinotopy predicts a responses to stimuli below 10° in the anterior 25% of V1.

Fitting was performed using a nonlinear, numeric log-error minimization technique on the spatially unsmoothed retinotopic data. Retinotopic data were filtered by F-statistic, and those vertices whose F-statistic was <8 were excluded (~90% of all brain vertices); although this threshold is extremely high, it should be noted that the F-statistics were calculated in reference to a mean model, thus are skewed very high. For eccentricity, the template was exponential along iso-angular bands (*i.e.*, eccentricity varied exponentially across iso-angular bands) with starting parameters adapted from Qiu *et al.* [16]. The template was given the form $r = 90º \exp(q(x - 1))$, where x is the coordinate of the iso-eccentric band passing through a particular point and q is the fit parameter. This form forced the template to have a value near (but not equal to) 0º at the posterior end of the V1 ellipse and a value of 90º at the anterior end of the V1 ellipse (**Table S1**). Vertices with eccentricity values within 2° of the outer stimulus boundary were excluded due to bias at the edge of the stimulus (Baseler *et al.*, [15]), and vertices with eccentricity values <2.5° were excluded due to the disorganization of retinotopy near the foveal confluence. For polar angle, the template was polynomial with a starting parameter of 1. The template was given the form $\theta = 90º + 90º \operatorname{sgn}(y) |y|^q$, where y is the coordinate of the iso-angular band passing through a particular point and q is the fit parameter. Aggregate templates were calculated by fitting templates to the entire dataset simultaneously.

Tests for structure-structure variability

The ability of the template to predict retinotopic organization is limited by several sources of variability and error. Primary among these is true structure-function variability, in which different subjects have (e.g.) a different relation between their retinotopic organization and the underlying anatomical landmarks. This type of variability is not directly measured by our data, but can be inferred from the presence of residual variability after two other sources of error are assessed. First, there may be structure-structure variability, in which residual differences in anatomical organization are not resolved by the cortical registration technique. Second, there may be error in the measurement of retinotopy in individual subjects, which limits the accuracy of even a perfect template. We considered the contribution of these sources of error to the prediction performance of our template.

We asked if anatomical registration differences could account for differences in template prediction performance. For each subject, we measured the root mean square deviation (RMSD) of their registered anatomical curvature from the template anatomy. Across subjects, RMSD values were tightly clustered in a normal distribution with mean 0.14 mm^{-1} and standard deviation 0.01 mm^{-1}. Small individual differences were visible across subjects, but the total range of the RMSD values was from 0.11-0.16 mm^{-1}. The RMSD measure did not correlate with the accuracy of polar angle or eccentricity predictions or with the template parameter values. This suggests that gross differences in anatomical registration between subjects do not account for a large portion of the template prediction error.

Tests for hemispheric variability

In the main text, we combined data from both hemispheres across subjects within a left-right symmetric template space. Here, we demonstrate that the similarity and independence of retinotopic measurements from the two hemispheres supports this practice.

Hemispheric differences in the organization of visual cortex have been reported previously. While left V1 tends to have a greater surface area [17], the right hemisphere contains a larger foveal confluence [18]. Significant within-subject differences between hemispheres in cortical magnification have been observed [16], although normalizing for surface area appears to result in cortical magnification functions from the two hemispheres with the same central tendency [18].

Because the spherical brain used in the creation of the V1 template is a symmetric pseudo-hemisphere that is equally similar to left and right hemispheres, RM data may be compared and potentially combined across hemispheres. In subject native space, left hemisphere V1 tends to have a larger cortical surface area [17]; this was observed in our population for the anatomically defined V1 region as well, and approached statistical significance [(LH) 2536 vs. (RH) 2339 mm^2, $t(25$ df$) = 1.74$, $p = 0.08$]. Normalization to the template space removes this difference, as well as the correlation in V1 size between the hemispheres that is present across subjects in native space [$r = 0.67$ in native space]. Our anatomically-based template allows similarities and differences in retinotopic representation between the hemispheres to be assessed after normalization for hemispheric differences in anatomy.

In both right and left hemispheres, a patch of low polar angle data was observed in the ventral anterior region of V1; this can be seen in **Figures 2A**, **2F** (inset), and **S2A** as a

blue patch near the upper right border of the plotted stimulus. Examination of the predicted polar angle and eccentricity template values for the vertices in this region revealed that the portion of the stimulus most likely corresponding to this region is a small band of ~7-10° eccentricity near the lower vertical meridian of the visual field. We determimed that this region of the display was partially obscured during our scans by two clamps, one on each side of the lower vertical meridian, that hold the head-coil mounted mirror in place. Although the bias from these clamps is small enough that we did not exclude it from our analyses, its effect can be seen in **Figures 2C** and **2D** where it contributes to the higher error in the range of 120-180° of polar angle.

Polar angle data for the right hemisphere were inverted and both polar angle and eccentricity templates fit exactly as in the left hemisphere. **Figures S2A** and **S2B** show the aggregate polar angle and eccentricity data for the right hemispheres in the 10º dataset while **Figures S2C** and **S2D** show the template fits, plotted as a function of a normalized axis. This axis, in the case of the polar angle template, represents elliptical iso-eccentric curves along the cortical surface normalized to be -1 at the point where the template predicts 0° of polar angle and 1 where the template predicts 180° of polar angle. For the eccentricity template, the axis represents hyperbolic iso-angular curves along the cortical surface normalized to be 0 where the template predicts (close to) 0° of eccentricity and 1 where the template predicts 90° of eccentricity. A single significant outlier subject (> 10 standard deviations from the mean) was excluded from this analysis in the case of polar angle; inspection of the data from this subject suggest that too few reliable vertices were available to provide a stable fit. The subject was not excluded from other analyses in this paper. Exact formulae and leave-one-out prediction median errors for each hemisphere, and the combined hemispheres, are given in **Table S1**.

Polar angle template parameters were not significantly different between hemispheres [paired t(24 df) = 1.51, p = 0.15, one significant outlier excluded], but eccentricity template parameters were significantly different [paired t(25 df) = 2.56, p = 0.02]. Despite this difference in the populations, it should be noted that the eccentricity template predictions for right and left hemispheres differ by <1.8° for all points in V1 (median absolute difference: 1.15°) and that neither right nor left template parameters have population means which differ significantly from the parameter of a template fit to all hemispheres combined [t_{RH}(25 df) = 1.84, p_{RH} = 0.08; t_{LH}(25 df) = 1.93, p_{LH} = 0.07].

Despite having similar central tendencies, there was a greater standard deviation for template fits in the right hemisphere, taken across individuals for both polar angle and eccentricity. This difference could not be attributed to worse anatomical registration in the right hemisphere. In fact, the RMSD of registered anatomy to the spherical brain was not significantly different in the right and left hemispheres [paired t(25 df) = 1.07, p = 0.28]. The greater right hemisphere variability could also not be explained by greater noise in measurement of retinotopy in the right hemisphere. The split halves analysis conducted in the right hemisphere for eccentricity produced essentially the same results as in the left hemisphere. We are therefore unable to reject the possibility that there is greater variability in the mapping of structure-function in right hemisphere V1.

Finally, we asked if variability between subjects in RM organization might be correlated across hemispheres within subject. This might occur if (*e.g.*) different subjects have different cortical eccentricity functions that are shared across hemispheres. To test this,

we calculated vertex-wise correlations in RM data between all hemispheres of all subjects in the measured eccentricity and polar angle data after anatomical normalization but without template fitting. We tested these correlations in RM information for statistically significant population differences between hemispheres and between subjects. As any hemisphere from any subject has a high correlation to any other hemisphere from any subject, we tested for population differences rather than examining the significance of the correlations themselves. All four populations (LH-LH correlations across subjects, RH-RH correlations across subjects, LH-RH correlations within subject, LH-RH correlations between subjects) had virtually identical distributions of correlation values and were not significantly different. We were unable to reject either the hypothesis that, after anatomical normalization, deviations from the population average are independent across subjects but dependent between the two hemispheres within a subject [p = 0.99] or the hypothesis that the deviations are independent between hemispheres of a single subject but dependent for the same hemisphere across subjects [p = 0.84].

  Although we find a difference in the cortical magnification for right and left hemispheres, the predicted differences in eccentricity are no larger than the error of a short fMRI scan (**Fig. S3D, E**). Additionally, we find that deviations in the retinotopic organization from the mean are independent across the two hemispheres. This has several implications. First, it suggests that the normalization approach is sufficient to remove the correlations in within-subject hemispheric variation that have been previously observed. Second, given that the two hemispheres share highly similar templates and that deviations from this template in the two hemispheres are independent, the retinotopic mapping data from the two hemispheres may be considered separate "subjects".

References

1. Dumoulin S.O. & Wandell B.A. (2008). Population receptive field estimates in human visual cortex. NeuroImage 39(2), 647-660.
2. Engel S.A., Glover G.H. & Wandell B.A. (1997). Retinotopic organization in human visual cortex and the special precision of functional MRI. Cereb. Cortex 7(2), 181-192.
3. Aguirre G.K., Zarahn E. & D'esposito M. (1998). The variability of human, BOLD hemodynamic responses. NeuroImage 8(4), 360-369.
4. Verstynen T.D. & Deshpande V. (2011). Using pulse oximetry to account for high and low frequency physiological artifacts in the BOLD signal. NeuroImage 55(4), 1633-1644.30.
5. Fischl B. & Dale A.M. (2000). Measuring the thickness of the human cerebral cortex from magnetic resonance images. Proc. Natl. Acad. Sci. USA 97(20), 11050-11055.
6. Dale A.M., Fischl B. & Sereno M.I. (1999) Cortical surface-based analysis I. Segmentation and surface reconstruction. NeuroImage 9(2): 179-194.
7. Salat D.H., Buckner R.L., Snyder A.Z., Greve D.N., Desikan R.S., Busa E., Morris J.C., Dale A.M. & Fischl B. (2004) Thinning of the cerebral cortex in aging. Cereb. Cortex 14(7): 721-730.
8. Fischl B., Sereno M.I., Tootell R.B. & Dale A.M. (1999) High-resolution intersubject averaging and a coordinate system for the cortical surface. Hum. Brain Mapp. 8(4): 272-284.
9. Greve D., Sabuncu M., Buckner R. & Fischl B. (2011). Automatic surface-based interhemispheric registration with FreeSurfer. Hum. Brain Mapp., Quebec City, Canada.
10. Hinds O.P., Rajendran N., Polimeni J., Augustinack J., Wiggins G., Wald L., Diana Rosas H., Potthast A., Schwartz El & Fischl B. (2008). Accurate prediction of V1 location from cortical folds in a surface coordinate system. NeuroImage 39(4), 1585–1599.
11. Schira M.M., Tyler C.W., Spehar B. & Breakspear M. (2010). Modeling magnification and anisotropy in the primate foveal confluence. PLoS Comp. Biol. 6(1), e1000651.
12. Balasubramanian M., Polimeni J. & Schwartz E.L. (2002) The V1-V2-V3 complex: quasiconformal dipole maps in primate striate and extra-striate cortex. Neural Networks 15(10):1157-1163.
13. Chaplin T.A., Yu H.H., Rosa M.G. (In Press) Representation of the visual field in the primary visual area of the marmoset monkey: Magnification factors, point-image size and proportionality to retinal ganglion cell density. J Comparative Neurology.
14. Press W.A., Brewer A.A., Dougherty R.F., Wade A.R. & Wandell B.A. (2001) Visual areas and spatial summation in human visual cortex. Vision Res. 41(10-11): 1321-1332.
15. Baseler H., Alyssa B.A., Sharpe L.T., Morland, A.B., Jägle H. & Wandell B.A. (2002) Reorganization of human cortical maps caused by inherited photoreceptor abnormalities. Nat. Neurosci. 5(4): 364-370.
16. Qiu A., Rosenau B.J., Greenberg A.S., Hurdal M.K., Barta P., Yantis S. & Miller M.I. (2006). Estimating linear cortical magnification in human primary visual cortex via dynamic programming. NeuroImage 31(1), 125–138.

17. Duncan O.D. & Boynton G.M. (2003). Cortical magnification within human primary visual cortex correlates with acuity thresholds. Neuron 38(4), 659-671.
18. Dougherty R.F., Koch V.M., Brewer A.A., Fischer B., Modersitzki J. & Wandell B.A. (2003). Visual field representations and locations of visual areas V1/2/3 in human visual cortex. J. Vis. 3(10), 586-598.